






A novel ultrasound-driven piezoelectric GBR membrane dispersed with boron nitride nanotubes promotes bone regeneration and anti-bacterial properties

Keshi Zhu^{a,1} , Ruixue Li^{b,a,1}, Shi Yin^{a,1} , Fei Yang^{a,c}, Yang Sun^a, Yixiao Xing^a, Yiling Yang^a, Wanjing Xu^a, Youcheng Yu^{a,b,*} 

^a Department of Stomatology, Zhongshan Hospital of Fudan University, Shanghai, China

^b Department of Stomatology, Xuhui Central Hospital, Shanghai, China

^c Department of Stomatology, Xiamen Branch, Zhongshan Hospital, Fudan University, Xiamen, China

ABSTRACT

Bone graft absorption and infection are the major challenges to guided bone regeneration (GBR), yet the GBR membrane is neither osteogenic nor antibacterial. Hence, we followed sono-piezo therapy strategy by fabricating an electrospun membrane dispersed with boron nitride nanotubes. The PLLA/Gelatine/PDA@BNNT (PGBT) membrane has improved mechanical and biocompatible properties and generate piezovoltages of 130 mV when activated by ultrasound stimulation under 100 mW/cm² without extra polarization. The PGBT with ultrasound is conducive to cellular osteogenesis, barrier function, and shows antibacterial rate of about 40%. The rat cranial defect experiments revealed that PGBT with ultrasound could promote osteogenesis in-vivo and show great potentials for vertical bone defect repair.

1. Introduction

Guided bone regeneration (GBR) is the mainstream clinical method for alveolar defect reconstruction, it exerts key effect through providing a hermetic and stable environment for bone healing by utilizing the GBR membrane, which fixes the bone graft and prevents fibroblasts invasion into the defect site [1]. However, rapid membrane degradation and bone graft absorption after surgeries frequently happen during alveolar remodeling period, with the absorption much faster than the osteogenesis, leading to unsatisfactory regenerative result. Moreover, oral cavity is a constant bacterial environment, postoperative infections easily occur [2]. Clinically, traditional GBR membrane is only a physical barrier without antibacterial and osteogenic activity. Researchers have made efforts to modify it via tissue engineering strategy, which involves the growth factor, exogenous seed cell and scaffold. However, various bioactive factors and cells work shortly because of explosive release, and have faced challenges such as immune responses, cell apoptosis, and high cost [3], these shortcomings have hindered the application of novel GBR membrane, a strategy that can work sustainably without mentioned cons is on demand. Simulating the bioelectric environment of human bone is recently introduced and studied [4]. Changes in bone's electrical

signals during movement play an important role in bone remodeling [5], and artificial electrical stimulation has been proven to produce similar bioelectrical signals [6], potentially enhancing cellular osteogenic differentiation and cellular activity through signaling pathways [7–9].

Sono-Piezo Therapy (SPT) is arousing scholars' increasing attention due to its non-invasiveness and controllability [10]. In SPT, artificial piezoelectric materials are activated through low intensity pulse ultrasound stimulation (LIPUS), then the generated electric potentials act as endogenous electric fields (EnEF) in human bone to assume a guiding function in osteogenesis [11]. Also, electric fields emanating from piezo-materials have been found to cause overwhelming potential differences and oxidative stress to bacteria, resulting its membrane breakage and death [12,13]. But previously, extensively researched bio-piezoelectric substances, such as barium titanate based materials and poly(vinylidene fluoride-trifluoroethylene) (P(VDF-TrFE)) based materials, are ferroelectric, which means that field polarization is required to charge the materials a intratissue "battery". It has limitations in duration [14] and faces challenges in internal application [15]. Moreover, barium titanate's high molecular mass makes it unsuitable for membrane fabrication, and P(VDF-TrFE) is limited in GBR due to its non-degradability [16,17]. People are searching for novel piezoelectric

* Corresponding author. Department of Stomatology, Zhongshan Hospital of Fudan University, Shanghai, China

E-mail address: yu.youcheng@zs-hospital.sh.cn (Y. Yu).

¹ represents co-author.

material to achieve the dual-function.

Boron nitride nanotube (BNNT), structurally similar to carbon nanotube but with different molecules [18], is recently discovered favorable piezoelectricity [19]. Relative literature reveals that it can be directly activated through ultrasound without polarization [20]. With a molecular weight one-tenth that of barium titanate, it is suitable for membrane fabricating. Limited researches on BNNT's application in tissue engineering, yet it notably enhances mesenchymal stem cell differentiation into osteoblasts [21], upregulates osteogenic gene expression [22,23], reduces reactive oxygen species (ROS) [24], induces hydroxyapatite deposition [25], promotes osteoblast adhesion and increases osteopontin output [26]. The potential mechanisms is highly possible to be related to its piezoelectricity [18,20]. Therefore, we choose BNNT to be an electrical growth factor and load it on scaffolds to construct a GBR membrane with SPT.

Electrospun membrane is viewed as an ideal scaffold. Poly-L-lactic acid (PLLA) based electrospun nanofibrous membrane is regarded as a promising strategy due to reticular structure and pore size like extracellular collagen matrix (ECM) [27,28]. PLLA itself is highly hydrophobic, literature reveals that the surface wetting behavior can improve with proper concentration of gelatin, since it provides considerable surface energy increases [29]. Meanwhile, electrospun PLLA has recently been found to reveal piezocatalytic response with asymmetric molecular structure [29,30], but its original piezoelectricity is insufficient for further biomedical applications and need strategies for enhancement [31,32].

In this study, PLLA and gelatin are selected to establish a scaffold, BNNT is added as a strong piezoelectric growth factor, to fabricate a novel GBR membrane with a pronounced piezoelectricity—PGBT membrane. The investigation delves into the application of LIPUS to PGBT in bone defect sites, generating dynamic, non-invasive, and quantifiable microcurrents. The mechanical, piezoelectrical and biological evaluation were implemented *in vitro*. We established a rat cranial defect model to evaluate the osteogenic potential of the PGBT membrane. The PGBT membrane is designed to enhance bone repair, eliminate local bacteria, and further explore the clinical potentials especially in dental implantation.

2. Materials and methods

2.1. Fabrication and preparation of the membrane

BNNT (Buwei, China) doped with 10 % wt dopamine (Sigma-Aldrich, PHR1090, USA) were mixed in 50 ml of Tris-HCl (pH 8.5) (Sigma-Aldrich, PHR9293, USA). After 24-h stir, the mixture solution turned black, indicating the polymerization of dopamine and the wrapping with BNNT. Following centrifugation at 1200 RPM for 10 min, the supernatant was discarded, and the process was repeated with distilled water washes thrice. The resultant sediment was oven-dried at 35 °C for 24h, then ground to obtain polydopamine-coated BNNT (PDA@BNNT) for subsequent use.

A mixture of 0.8g PLLA (Daigang Bio, China), 0.2g Type A gelatine (Sigma-Aldrich, V900863, USA), and 50 mg PDA@BNNT were dissolved in 10 ml hexafluoro isopropanol (Sigma-Aldrich, 105228, USA) and stirred for 12h. This mixture was electrospun by feeding it through a high-voltage needle (16 kV) at a flow rate of 2 ml/h onto a collector rotating at 1200 rpm, 18 cm away, under conditions of 26 °C and 50 % humidity. The membrane was dried at room temperature for 3 days and collected. Samples were cut into circles with the same diameter of plate's well. All samples were treated under ultraviolet 4h for both sides and then immersed in 75 % ethanol before *in-vitro* experiment.

2.2. Characteristics of membrane

2.2.1. SEM and EDS observation

The fiber membrane was sputter-coated with gold for 45s and then

observed under a scanning electron microscope (SEM) (Thermo Fisher, Phenom Pharos G2, USA) at a voltage of 10 kV for morphological analysis. Subsequently, the sample underwent region and mapping scan using an energy-dispersive X-ray spectroscopy (EDS) (Thermo Fisher, Phenom Pharos G2, USA) to determine its elemental composition and distribution.

2.2.2. Piezoelectricity

For piezoelectricity, the circular membrane of a diameter of 3.4 cm was sandwiched between two silver electrodes (>99.99 %, KSR Mater, China) of the same size, and double-sided copper leads were soldered to it. The leads were connected to an oscilloscope (UNI-T, UPO2202, USA). The assembly of electrodes with no membrane was set as blank group to measure the noise voltage value from unexpected triboeffect, the assembly of electrodes with PLLA/gelatine membrane was set as Control group, and the assembly of electrodes with PGBT membrane was set as PGBT group. Each assembly was tightly encapsulated with polytetrafluoroethylene tape and firmly fixed to the ground to avoid triboeffect noise. An ultrasound therapy device (WELLD, WED-100, China), with its treatment probe fully coated with coupling agent in case of vibration heat noise, was solidly positioned parallel and 0.5 cm above the element. The ultrasound intensity was set as 0.1W/cm². The peak-to-peak voltage of each group was recorded and referred to as maximum voltage. Blank group's peak-to-peak voltage was named as noise voltage value, and the actual piezovoltage of Control and PGBT groups were calculated as maximum voltage value subtract the noise value.

2.2.3. Mechanical, hydrophilicity and degradation test

Membranes were cut into strips and clamped at both ends under a universal testing machine (Instron, 3400, USA) at 22 °C, with a tensile speed set at 5 mm/min. The elastic modulus and tensile strength were calculated.

Membranes were placed under a contact angle goniometer (Sindin, SCD-200, China). A droplet of 10 μl distilled water was dropped onto the material surface from 1 cm above, and the water contact angle at 5s was automatically measured using Nanodrop software to assess material hydrophilicity (n = 3).

For degradation rate experiments, film samples were cut, weighed for initial weight (W₀), and immersed in artificial saliva, with the solution changed weekly. Samples were retrieved at 2, 4, 6, and 8 weeks, rinsed with deionized water, dried at 37 °C for 12h, and weighed for the final weight (W_t). The degradation rate percentage was calculated as follows:

$$\text{Degradation rate (\%)} = (W_0 - W_t) / W_0 * 100\%$$

2.3. Bone regeneration evaluation *in-vitro*

2.3.1. Cell culture and seeding

MC3T3-E1 and NIH3T3-E1 cells were cultured in complete medium, composed of DMEM, fetal bovine serum, penicillin and streptomycin. Then they were incubated at 37 °C in a 5 % CO₂, ensuring sterile techniques throughout to prevent contamination. When the confluency reached 80 %, cells were passaged at a ratio of 1:3. Membranes were cut and sterilized, then placed in a 24-well plate, secured with stainless steel rings. 2 × 10⁴ MC3T3-E1 cells were added to each well, and the plate was gently swirled to mix. The complete culture medium was replaced every two days.

For LIPUS groups, The WELLD ultrasound probe was mounted 0.5 cm below the plate with coupling agent filling the gap, targeted well bottom was parallel to and aligned with the center of the ultrasound probe. LIPUS was applied at an intensity of 0.1W/cm² with a duty cycle of 20 ms for 5 min per session, every two days.

2.3.2. Cell viability assay

2.3.2.1. Leachate viability assay. Membranes were put in wells and co-incubated with culture medium at 37 °C for 3 days to collect the leachate. Then MC3T3-E1 cells were passaged and seeded in to 96-well plate. On the day of 1, 3, 5, the leachate were updated and 10 wt% CCK-8 reagent (Dojindo, CK04, Japan) was added, the plates were incubated for 2 h, then the absorbance at 450 nm was measured using a microplate reader (Thermo Fisher, Varioskan ALF, USA).

2.3.2.2. Co-cultivation viability assay. 1, 3, 5 days after cells were seeded on the membranes, culture medium was refreshed and 10 wt% CCK-8 reagent (Dojindo, CK04, Japan) were added. After gentle shaking and 2 h of incubation, the suspension was homogenized by pipetting, and 200 µl of the suspension was transferred to a 96-well plate for absorbance measurement at 450 nm.

2.3.2.3. Live/dead staining. On the 3rd day after seeding, samples were rinsed with PBS. A staining solution of Calcein (AM)/Propidium Iodide (PI) (Beyotime, China) was prepared and added to each well, followed by incubation in the dark at 37 °C for 30 min. Confocal microscopy (Olympus, SpinSR10, Japan) was employed to capture images, setting the excitation wavelength at 530 nm for AM and 645 nm for PI.

2.3.3. Cell adhesion observation

2.3.3.1. SEM. On the 3rd day after seeding, samples were rinsed and then fixed in 4 % paraformaldehyde (PFA) at 4 °C for 4 h. Dehydration was performed using a graded series of ethanol concentrations (30 %, 50 %, 70 %, 90 %) for 15 min each, followed by two 15-min treatments with 100 % ethanol. After air-drying at room temperature, samples were sputter-coated with gold for 45 s and observed under SEM.

2.3.3.2. Staining. On the 3rd day of co-culture, samples were fixed with 4 % paraformaldehyde (PFA) at 4 °C for 10 min, followed by two PBS washes. Then they were permeabilized with 1 ml of 0.1 % Triton X-100 solution for 10 min and washed. A phalloidin/DAPI (Beyotime, China) staining was applied under kit guidance. Confocal microscopy's imaging settings were adjusted to a phalloidin excitation wavelength of 555 nm and a DAPI excitation wavelength of 488 nm to capture the images.

2.3.4. Osteogenic induction staining

2.3.4.1. Medium preparation and osteogenic induction. DMEM and α -MEM in a 4:1 ratio, supplemented with 10 mM β -glycerophosphate, 0.25 mM ascorbic acid, and 10^7 M dexamethasone, were mixed for osteogenic induction. MC3T3-E1 cells were cultured until 80 % confluency, then switched to osteogenic medium every 3 days.

2.3.4.2. Alkaline Phosphatase (ALP) staining. After 14 days, samples were washed and fixed, stained with NBT/BCIP working solution from an ALP kit (Beyotime, China) for 1 h in the dark. Then they were rinsed, dried and imaged under microscope. For quantification, 1 ml of 10 % w/v cetylpyridinium chloride was added per well for 1 h, and 200 µl of the solution was measured at 570 nm.

2.3.4.3. Alizarin red (AR) staining. After 21 days, samples were rinsed and fixed with 4 % PFA for 30 min, washed with deionized water. Then they were stained with 1 ml AR solution from an AR kit (Beyotime, China) for 20 min at room temperature and imaged. For quantification, 1 ml of 10 % w/v cetylpyridinium chloride was added per well for 1 h, and 200 µl of the solution was measured at 570 nm.

2.3.5. Barrier function assessment

Fiber membranes were and placed in Transwell chambers and

NIH3T3-E1 cells (2×10^4 cells/well) were seeded. Medium was changed every two days. After 14 days, samples were fixed with 4 % PFA, dehydrated in ethanol, and air-dried, then embedded, sectioned, and stained with hematoxylin. Sections were observed and imaged under a microscope to assess cell distribution and membrane's barrier effect.

2.4. Anti-bacterial evaluation

2.4.1. Colony counting

Escherichia coli (*E. Coli*) was grown in LB medium at 37 °C on a shaker for 12 h and adjusted to a concentration of 10^7 CFU/ml. 10 µl of this bacterial suspension and 1 ml of LB medium were added to a 24-well plate with a fiber membrane. The ultrasonic group was treated using a LIPUS probe at the bottom of the plate, providing a stimulation of 0.1 W/cm² for 5 min. The suspension from the plate was diluted 100 times, plated on agar, and incubated at 37 °C for 24 h. Colonies were photographed, counted using ImageJ software, and the antibacterial rate was calculated.

2.4.2. CCK-8

E. Coli suspension was treated as before. The suspension from the plate was diluted 1000 times and 100 µl suspension was added into 96-well plate and 10 µl CCK-8 reagent was added into each well. The plate was cultured in 37 °C for 2h, then the absorbance at 450 nm was measured using a microplate reader.

2.5. Bone regeneration in-vivo

2.5.1. Animal experiment

The in-vivo experiments were censored and approved by the Animal Ethics Committee of Zhongshan Hospital, Fudan University, Shanghai, China (No. 2023-296). Six-week-old male SD rats weighing between 150g and 200g were provided by Animal Experiment Center of Zhongshan Hospital, Fudan University. All rats were fasted for 4 h and then anesthetized with a 1 mg/kg intraperitoneal injection of 2 % pentobarbital sodium. Following aseptic preparation, longitudinal incision was made at the midline of the skull. Circular defects, 6 mm in diameter and matching the full thickness of the skull bone, were created on both the left and right sides of the skull using a cooled trephine drill under saline irrigation. Care was taken to avoid damages.

The rats were divided into two time groups, 4-week and 8-week, with 15 rats for each. Each time group included: untreated blank group (B), Control membrane coated without ultrasound (C-), Control membrane coated with ultrasound (C+), PGBT Membrane coated without ultrasound (P-), and PGBT Membrane coated with ultrasound (P+), n = 6. 1 week after surgery, rats in the ultrasound groups were immobilized in a custom fixture, and ultrasound stimulation was applied using ultrasound probe at 0.1 W/cm² for 5 min, twice a week. At 4 and 8 weeks post-surgery, rats were euthanized under anesthesia.

2.5.2. Micro-CT evaluation

The bone defect area was carefully dissected and underwent Micro-CT scanning (SKYSCAN 1276, Bruker, German). The scanning was under 90 kV voltage, 90 µA current, and the voxel resolution was 50 µm. Analysis software (3D.SUITE, Bruker, German) was used to evaluate bone/total volume ratio (BV/TV) and bone mineral density (BMD) of the defect area.

2.5.3. Histological assessment

Heart, liver, spleen, lungs, and kidneys were collected and fixed in tissue fixation solution, hematoxylin and eosin (HE) staining is applied to access the biocompatibility in-vivo.

After Micro-CT scanning, bone tissues underwent fixation, decalcification, dehydration, and xylene infiltration. They were then embedded in paraffin, sectioned, and stained with HE, Masson staining, and Immunohistochemistry (IHC). For IHC, samples were first incubated

with primary antibodies (OCN, Col-I) overnight at 4 °C, followed by secondary mouse IgG antibodies for 50 min at room temperature. DAB chromogen was applied until tissue staining appeared brown-red.

3. Results

3.1. Illustration of the fabrication of PGBT membrane

The fabrication procedures of the electrospun PGBT membrane are showed in Fig. 1A.

3.2. Characterization of the PGBT membrane

Scanning electron microscopy (SEM) results (Fig. 1B) revealed that BNNTs exhibit a tubular structure with lengths of approximately 20 μm and diameters ranging from 200 nm to 1 μm . Following the addition of dopamine, clusters of polydopamine encapsulating BNNTs were observed.

The SEM observations of the electrospun fiber membrane were presented in Fig. 1C. The control group's PLLA/gelatin electrospun membrane exhibited an interlaced network structure with uniform diameters and smooth surfaces. Upon the mixture of PDA@BNNT, no significant changes in the morphology were observed, with a small number of larger-diameter BNNT short tubes failed to be encapsulated by the nanofibers and adhering to them. Energy-dispersive X-ray spectroscopy (EDS) (Fig. 1B) revealed the scattered distribution of nitrogen and boron elements, indicating their uniform encapsulation within the nanofiber membrane. The overall area map-scan results indicated that the contents of nitrogen and boron elements are 3.86 % and 3.45 % respectively, in accordance with experiment design.

Mechanical test (Fig. 1C,D) showed that the average tensile strength of the control group's fiber membrane was 1.54 MPa, while that of the

PGBT group was 2.20 MPa, but with no significant difference. After the addition of BNNT, the elastic modulus of the material underwent a 69.5 % boost, from 24.6 MPa to 41.69 MPa ($p < 0.5$).

Hydrophilicity test (Fig. 1E) showed that at the fifth second after the water drop contacted the material, the average instantaneous water contact angles of the PGBT group and the control group were 33.78° and 32.22°, respectively, both demonstrating good hydrophilicity. After 5s, the water droplet was gradually completely absorbed.

Degradation tests (Fig. 1F) indicated that the dissolution rates of PGBT and the control group were faster in the first two months, with dissolution rates of 32.68 % and 32.34 % at 15 days, and 51.28 % and 47.67 % at 30 days, with no statistical significance in the differences. Subsequently, the dissolution rates of both groups gradually slow down. By the 90th day, the dissolution rates between the two groups were 72.08 % and 61.71 % ($p < 0.05$). Afterwards, experimental data could no longer be obtained. Overall, the dissolution rate of the PGBT was slightly faster than that of the control group, with complete dissolution occurring around the third month.

Fig. 1G presented the piezoelectric properties of the nanofiber membrane material. Two electrode plates were first attached directly without membrane, then a LIPUS stimulation of 0.1 W/cm² was applied to them. The maximum voltage of blank group was recorded 24 mV, as shown in Fig. 1G(a). This was perceived of the noise generated from the triboeffect of the silver electrode, copper wire, and polytetrafluoroethylene tape, so the maximum output voltages of the control group and the PGBT group were subtracted from this noise value to obtain the actual ones. Fig. 1G(b) showed that after the control group's membrane is connected to the electrode plate and the same intensity LIPUS stimulation is applied, the maximum output voltage is 38 mV, and the actual output voltage should be 14 mV. Fig. 1G(c) showed that when the same intensity LIPUS stimulation was applied to the PGBT group, the maximum output voltage is 154 mV, and the actual output voltage

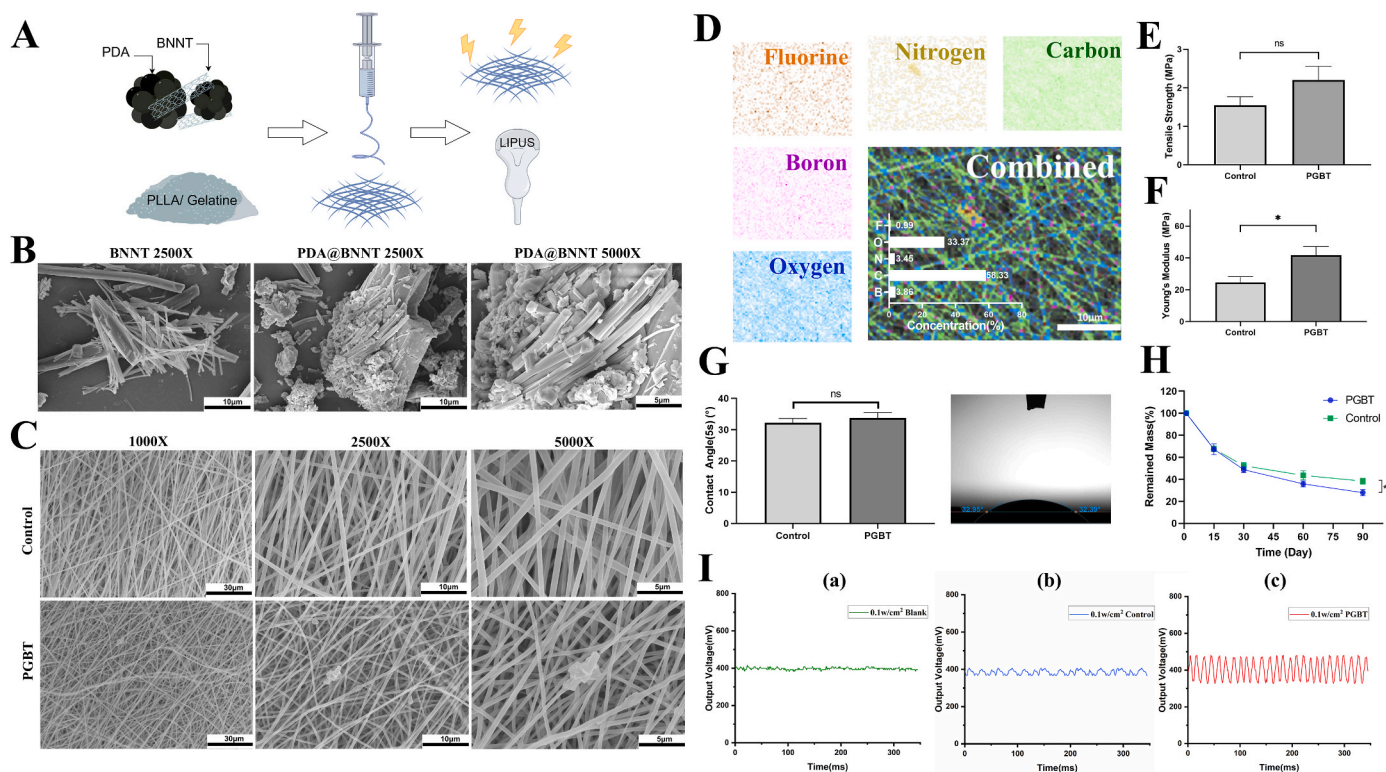


Fig. 1. Morphology and characteristics of membranes. (A) Abstract of membrane fabrication. (B) SEM images of BNNT and PDA@BNNT. (C) SEM images of control and PGBT groups. (D) Energy-dispersive spectroscopy evaluation of PGBT membrane (E, F) The tensile strength and Young's modulus of the membranes (G) Hydrophilicity test of membrane. (H) Weight loss of the membranes in PBS solution. (I) Output voltage of (a) blank group, (b) control group, (c) PGBT group under LIPUS.

should be 130 mV.

3.3. Biological evaluation of the PGBT membrane in vitro

3.1 The illustration picture showed that cells are directly seeded on the electrospun membrane, which was fixed in the well through the stainless ring and cultured in medium. LIPUS was applied by an ultrasound probe beneath the plate.

3.3.1. Biocompatibility and cell viability

Live/dead bacterial staining experiments (Fig. 2B) demonstrated that all four groups of cells on the membranes exhibited significant calcein green fluorescence intensity, indicating good cell viability. Bare cell death was observed, and there were no significant differences between the groups, confirming the good biocompatibility of the material and its suitability for cell colonization. The CCK-8 experiments of the membrane extraction solution and co-cultured cell and membrane

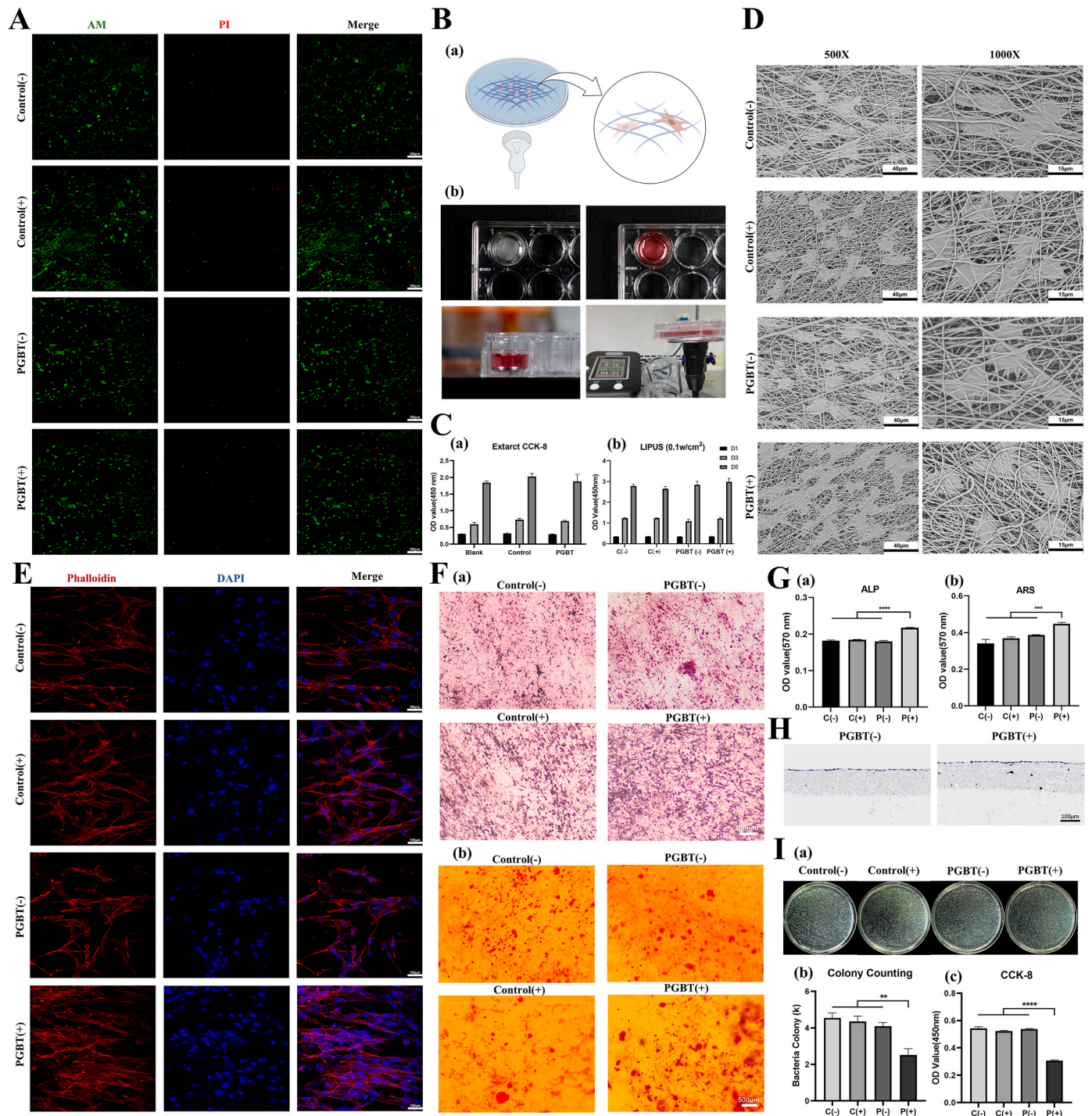


Fig. 2. Biological evaluations of the membranes. (A) Live/dead staining confocal microscopy images after the co-culture of cells and PGBT membrane. (B (a–b)) Illustration of cell seeding on PGBT membrane and LIPUS treatment. (C) (a) Leachate cell viability assay, (b) Co-cultivation viability assay. (D) SEM images of cell adhesion to membrane. (E) phalloidin/DAPI staining on focal microscopy images of cell adhesion to membrane. (F) (a) ALP staining images, (b) AR staining images. (G (a–b)) Quantitative analysis of ALP and AR staining. (H) Barrier function assessment of membranes. (I) Antibacterial evaluation of membranes, (a) Colony counting wells, (b) Analyzed bacterial colony, (c) CCK-8 analysis of bacterial suspension.

(Fig. 2Ca,b) showed that neither the different materials nor the ultrasound treatment affect the proliferative vitality of the cells, and there were no statistical differences between the groups.

3.3.2. Cell morphology observation

To observe the specific morphology of the cells colonized on the fibrous membrane, the materials co-cultured with the cells were fixed and gold sprayed for SEM observation (Fig. 2D). The fibrous morphology of the different materials and different ultrasound treatment groups showed no significant changes and is distributed in an interwoven network. The cell pseudopodia are visible, extending and located between the fibrous filaments, and the overall polygonal shape is attached to the fibrous membrane. The PGBT (+) group showed a higher cell density than the other groups, suggesting that ultrasound treatment of PGBT increased cell adhesion and aggregation. The DAPI/Phalloidin staining experiment demonstrated consistent results, with MC3T3-E1 cells showing polygonal distribution, and the cell density of the PGBT (+) group increased, suggesting an improvement in adhesion (Fig. 2E).

3.3.3. Osteogenic induction differentiation of MC3T3-E1

To further illustrate the level of osteogenic differentiation of cells after different materials and ultrasound stimulation, ALP and AR staining and semi-quantitative analysis were performed on MC3T3-E1 osteogenic induction for 14 and 21 days. As shown in Fig. 2F(a), the ALP staining level of the PGBT (+) group was the highest. It suggested that after 14 days of osteogenic induction on the PGBT membrane and application of 0.1w/cm² ultrasound stimulation for 5 min/time, twice/day, the osteogenic differentiation of the cells was higher than the other groups. As shown in Fig. 2F(b), the AR staining level of the PGBT (+) group was significantly higher than the other groups, suggesting that after the cells are osteogenically induced on the PGBT membrane for 14 days and ultrasound stimulation was applied, the mineralization of the cells was higher than the other groups. As shown in Fig. G(a, b), the semi-quantitative analysis of osteogenic induction staining showed that the ALP and AR staining levels of PGBT(+) were significantly higher than the other groups, and there were no statistical differences between the other groups.

3.3.4. Barrier experiment

To detect the barrier effect of the barrier membrane on fibroblasts, NIH3T3-E1 cells were co-cultured with the PGBT membrane for experiment (Fig. 2H). The cross-section of the stained material shows that NIH3T3-E1 cells in both the ultrasound and non-ultrasound groups were distributed on the surface of the fibrous membrane, and no cells were seen to penetrate and fall through the fibrous membrane. The experimental results suggested that the PGBT membrane had good soft tissue shielding performance.

3.3.5. Antibacterial properties

Firstly, *E. coli* is co-cultured with the cell membrane and a colony experiment was conducted to detect the antibacterial properties of the fibrous membrane. As shown in Fig. 2I(a), the Control(-), Control(+), PGBT(-) groups had more bacterial colonies and a larger colony density, but those in the PGBT(+) group significantly reduced. The cell count results (Fig. 2I(b)) showed that the number of bacterial colonies in the PGBT(+) group is significantly lower than the other three groups ($p < 0.01$), and the antibacterial rate reached 42.21 % compared to the Control group. The CCK8 test after co-culturing *E. coli* and the fibrous membrane showed a result in accordance with the colony test, with the OD value of the bacterial solution in the PGBT(+) group falling by about 43.03 % compared to the other three groups. This study suggested that the PGBT membrane combined with LIPUS stimulation has good antibacterial properties, with an antibacterial rate of about 40 %.

3.4. Osteogenic evaluation in vivo

4.1 Illustration of the operation and LIPUS treatment is depicted in Fig.B.

3.4.1. Micro-CT scanning and analysis

The micro-CT scanning of the skulls 4-week after surgery were shown in Fig. 3A(a), in Blank group, there was no obvious new tissue observed in the range of defects, and only a small part of new bone is visible at the edge of the defect. The coronal section showed a void in the skull defect, and the height of the new bone at the edge was not obvious. In the Control(-), Control(+), and PGBT(-) groups, about 20 % of the defect area was filled with new bone, mainly distributed in the center and edge of the circular defect. The three-dimensional reconstruction showed that the new bone presents a loose porous network structure, consistent with the morphological structure of the fibrous membrane. The regional coronal section showed the bone plate line and low-density image of the loose state, and the height of the new bone reaches about half of the surrounding bone height. In the PGCT(+) group, newly generated bone covered about 60 % of the defect area, mainly distributed in the center of the defect, and the density significantly increases compared to the other groups. The coronal section showed that the bone plate line at the bottom of the defect is more continuous than the others, and the height is more consistent with the level of the surroundings. It suggested that in the early stage of osteogenesis, PGBT + LIPUS can significantly promote bone regeneration.

Skulls at week 8 post-surgery were shown in Fig. 3A(b), in the Blank group, there was more new bone at the edge of the skull defect, gradually healing towards the center, but still with large defects. In the Control(-), Control(+), PGBT(-) groups, 60–80 % of the area is covered by new bone tissue, and only a part of the area stores bone defects. The coronal section showed that the height of the new bone is consistent with the level of the surrounding bone, and the bone plate at the bottom of the defect area is more continuous, but there were still some areas not fully filled. In the PGBT(+) group, the defect area was completely fulfilled with new bone, the coronal section showed that the it is more complete, and the density is high. The height of the new bone in some areas even exceeded the surroundings, achieving the regeneration of vertical bone defects beyond expectation.

As shown in Fig. 3C(a,c), the 4-week BV/TV of the PGBT(+) group was 14.07 %, significantly higher than the other four groups ($p < 0.01$). There was no statistical difference between the Control(-), Control(+), PGBT(-) groups. Compared to the control group, the PGBT(+)'s BV/TV is 25.04 % higher. The BMD of PGBT(+) is 0.3952 g/cm³, statically higher than the other four groups ($p < 0.05$), and was about 31.56 % higher than the control group. At week 8, the BV/TV of PGBT(+) was 23.79 % (Fig. 3C(b)), significantly higher than the others ($p < 0.01$), and the increase is 45.24 % compared to the control. BMD also showed similar experimental results (Fig. 3C(d)), the BMD of the PGBT(+) group was 0.6061 g/cm³, an increase of 14.77 % compared to the control ($p < 0.01$). The above results suggested that the bone quality after PGBT membrane is applied with LIPUS stimulation is better.

3.4.2. HE staining of major organs

To evaluate the potential biotoxicity of the material, we performed HE staining on the heart, liver, lungs, spleen, and kidneys of rats. At 8 weeks, we observed the pathological changes in the organs of rats implanted with PGBT. The results (Fig. 4A) showed no significant inflammatory response or pathological phenomena in any of the organs.

3.4.3. HE & Masson staining results**

At weeks 4 and 8, we conducted HE and Masson staining experiments to assess the repair of bone defects. The results at 4 weeks (Fig. 4B(a), Fig. 4C(a)) showed that in the Blank group, due to the invasion of a large amount of soft tissue, the bone defect area appeared concave, mainly showing fibrous healing, with no obvious new bone tissue. In the Control

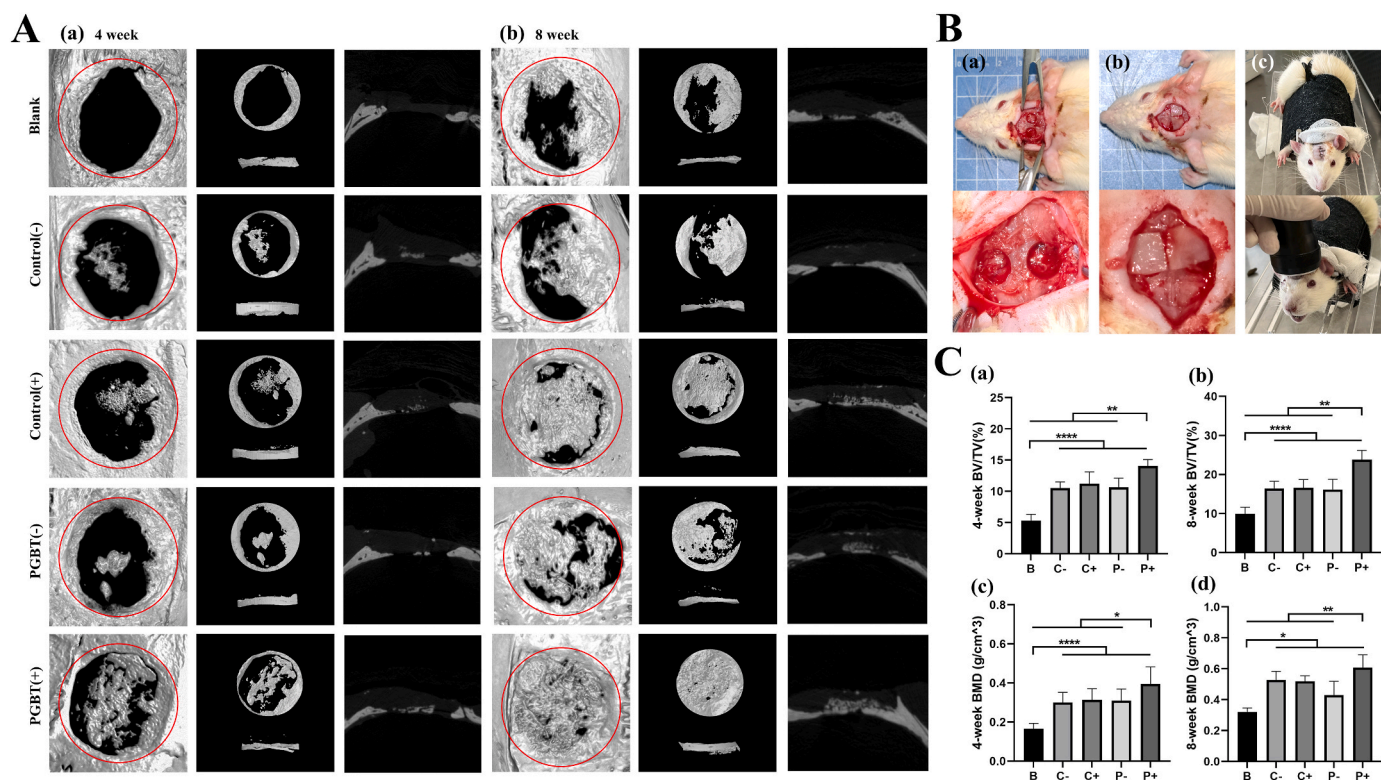


Fig. 3. Radiological evaluation in rat cranial defect regeneration. (A)(a–b) Reconstructed three-dimensional Micro-CT images at 4 and 8 weeks after the membrane covered defect sites. The margin of defected bone was marked with red cycle. (B) (a) 6 mm rat cranial defect model, (b) surgical procedure, (c) LIPUS treatment. (C(a–d)) Analyzed bone tissue parameters of bone mineral density (BMD) and the ratio of bone volume to tissue volume (BV/TV) from blank, control(–), control(+), PGBT(–), and PGBT(+) groups (*, $p < 0.05$, **, $p < 0.01$).

(–), Control(+), PGBT(–), and PGBT(+) groups, the barrier membrane covering the upper edge can be observed, maintaining good spatial morphology of the defect area. In the Control(–) and PGBT(–) groups, a significant amount of new bone tissue grew from the periphery to the center of the defect bottom, while in the Control(+) group, a small amount of new bone tissue was evenly distributed in the defect area with no significant aggregation at the bottom. In the PGBT(+) group, significantly more new bone was observed, mainly distributed in the center of the defect area, showing a vertical growth structure, with no obvious bone plate at the bottom and edges of the defect area. The internal structure of the new bone in the Control(–), PGBT(–), and PGBT(+) groups showed more bone marrow-like tissue structure compared to the Control(+) group. Additionally, HE staining in the Blank group showed a significant aggregation of inflammatory cells, while no significant inflammatory cell infiltration was observed in the other groups.

At 8 weeks (Fig. 4B(b), Fig. 4C(b)), the morphology of the defect area in the Blank group showed significant recovery, with a thin layer of loose new bone forming at the bottom, and new bone from the periphery converging towards the center. In the Control(–) and PGBT(–) groups, a relatively continuous thick layer of new bone tissue was observed at the bottom of the defect area, with a clear new bone marrow cavity. The height of the new bone decreases from the higher peripheral area towards the center, with the height central area reaching about half of the surrounding bone tissue. In the Control(+) group, the new bone structure was uniformly distributed, with increased density compared to 4 weeks, and no significant continuous bone plate was observed at the bottom of the defect. However, a continuous mass of high-density new bone was seen in the center of the defect area. The results in the PGBT(+) group showed a large amount of continuously distributed high-density new bone structure in the defect area, with a significant bone marrow structure, presenting a vertical large-scale bone repair. The height of the new bone recovered to the level of the surrounding bone,

even exceeding the original bone height in some areas. However, the new bone at the bottom of the defect was relatively general, without forming a complete continuous bone plate. No inflammatory cell infiltration was observed in any of the groups.

As shown in Fig. 4F(a), the trends in the results at 4 and 8 weeks were consistent: the new bone area in the PGBT(+) group was significantly higher than in the other groups, with statistically significant differences. At 4 weeks, the new bone area in the PGBT(+) group increased by approximately 30% compared to the Control(–), Control(+), and PGBT(–) groups, and at 8 weeks, it increased by approximately 74%.

3.4.4. Immunohistochemical staining

3.4.4.1. Type I collagen.** To verify the expression of osteogenic proteins in the newly formed bone tissue in the defect area, we performed immunohistochemical staining for type I collagen (Collagen-I, Col-I). As shown in Fig. 4D(a), at 4 weeks, the Blank group showed no new bone formation, with only partial fibrous positive expression in the upper layer of the defect area. In the Control(–), Control(+), and PGBT(–) groups, positive expression of Col-I was observed in the bone tissue, consistent with the results shown by HE & Masson staining. The PGBT(+) group had the highest area of positive regions, with positive new bone tissue located below the fibrous membrane, interweaving with the fibrous membrane. The local magnified image showed that the fibrous filaments under the nanomembrane are interwoven into the new bone. At 8 weeks, the Blank group showed partial positive expression of new bone at the bottom, and the Control(–), Control(+), and PGBT(–) groups proved increased positive expression of Col-I in the bone tissue. The PGBT(+) group indicated a large area of positive expression. Semi-quantitative test results (Fig. F(b)) showed that the area proportion of Col-I positive expression was significantly higher in the PGBT(+) group than in the other groups, with an increase of about 52% at 4 weeks and

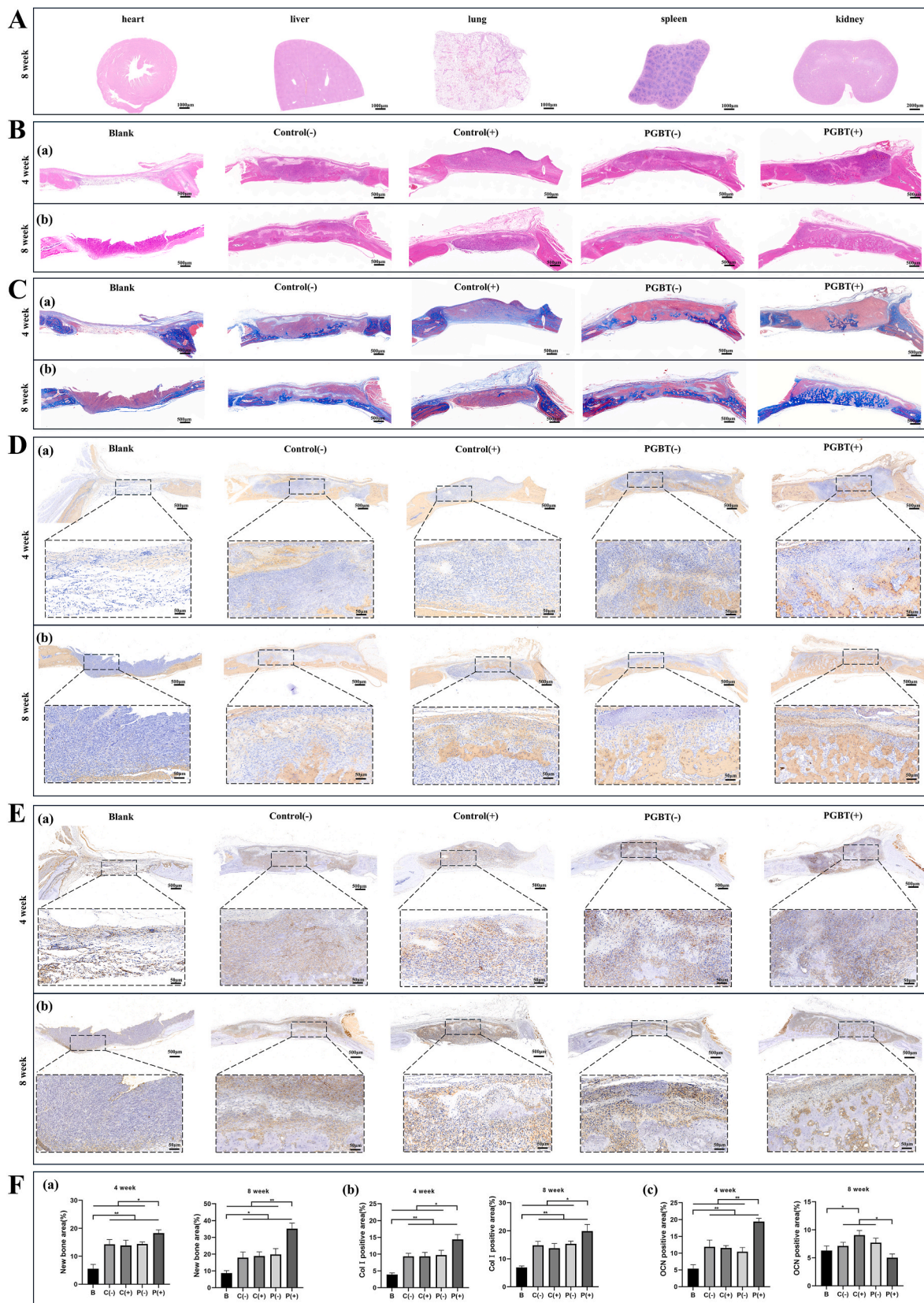


Fig. 4. Histological evaluation of organs and rat cranial bone regeneration. (A) 8-week cytotoxicity evaluation. HE staining sections of rat heart, liver, lung, spleen, and kidney. (B) 4-week(a) and 8-week(b) HE staining sections of defect bone regeneration. (C) 4-week(a) and 8-week(b) Masson staining sections of defect bone regeneration. (D) 4-week(a) and 8-week(b) Type I collagen immunohistochemical staining sections of defect bone regeneration. The selected region was lined with blank rectangle and zoomed in ten times below. (E) 4-week(a) and 8-week(b) Osteocalcin immunohistochemical staining sections of defect bone regeneration. The selected region was lined with blank rectangle and zoomed in ten times below. (F) (a) Quantitative analysis of new bone area. (b) Quantitative analysis of type I collagen. (c) Quantitative analysis of osteocalcin. (*, $p < 0.05$, **, $p < 0.01$).

about 43 % at 8 weeks compared to the Control(-), Control(+), and PGBT(-) groups.

3.4.4.2. Osteocalcin. Osteocalcin (OCN) is a non-collagenous protein secreted by osteoblasts. We performed immunohistochemical staining for the OCN marker, and the results are shown in Fig. 4E. At 4 weeks, the Blank group showed a small amount of loose positive cells at the bottom. In the Control(-), Control(+), and PGBT(-) groups, a larger number of positive cells were observed in the defect area, evenly distributed. The PGBT(+) group showed strong positivity, with the largest area proportion of OCN expression. Semi-quantitative analysis results showed that the area proportion of positive expression in the PGBT(+) group is significantly higher than in the other groups, with an increase of about 62 % compared to the other three groups. At 8 weeks, the positive proportion in the Blank group increased, and semi-quantitative results (Fig. F(c)) showed no significant difference between the Blank, Control (-), and PGBT(-) groups, but significantly lower than the Control(+) group ($p < 0.05$). The PGBT(+) group results were significantly lower than the Control(-), Control(+), and PGBT(-) groups ($p < 0.05$).

4. Discussion

Electrospinning is an efficient method for constructing fibrous membrane scaffolds, offering the most vital advantage of a porous network structure similar to ECM that allows for the free exchange of nutrients and metabolic products necessary for cell growth, facilitating cell proliferation and differentiation [33]. Researchers have incorporated various bioactive components, including osteogenic, chondrogenic, vascular, and antimicrobial component [34], into electrospun membranes. However, the efficacy of these components is short-lived due to their rapid release, preventing sustained effects [34]. Additionally, current strategies are excessively intricate and costly, hindering widespread clinical application. The development of piezoelectric materials offers a solution to this problem. In sono-piezo therapy, piezoelectric materials need to be uniformly distributed on the biological scaffold material and produce effects when stimulated by ultrasound. In this study, we incorporated boron nitride nanotubes into PLLA/gelatin to construct electrospun membranes, characterized their physicochemical properties, and tested the biocompatibility, cell adhesion, barrier performance, and antibacterial properties of the fibrous membranes *in vitro*. The osteogenic potential of the fibrous membranes was tested in both *in-vivo* and *in-vitro* experiments.

Nanomaterials exhibit poor dispersion in liquids and tend to sediment and agglomerate [35]. Dopamine-coating is reported an effective approach to increase surface energy of nanomaterials and improve the dispersion [36], relative researches also reveal that dopamine is conductive to osteogenesis and biocompatibility [37,38]. Therefore, we take advantage of dopamine to acquire PDA@BNNT and make it evenly distribute in the matrix solution. As shown in Fig. 1B, the electron microscopy images of BNNT and PDA@BNNT indicate that the nanotubes are wrapped and encapsulated by polydopamine clusters. The surface morphology of the fibrous membrane significantly affects cell adhesion and proliferation, with uniform and stable fibers being a basic requirement. In this experiment (Fig. 1C), both the control group and the PGBT group exhibit uniform morphology and smooth surfaces, with no obvious bead formation or clumping. The fiber diameter of PGBT slightly decreases, and a small amount of nanotube agglomeration is observed without being encapsulated by the fibers, but the overall morphology remains unchanged. Energy spectrum analysis shows that the average content of B and N elements is 3.66 %, which is consistent with the experimental design. The concentration of PDA@BNNT is sifted out through biocompatible and piezoelectric evaluation (Supplementary Data).

GBR membranes require excellent mechanical properties to maintain integrity during surgery and withstand internal and external tensions

during oral activities [39]. Our results show that the addition of BNNT improves the tensile property and elastic modulus of the material, it may be attributed to nanotube's inherent strength and increased intermolecular interaction of the membrane. Studies elucidated that carbon nanotubes provide electrospun membrane with more C-H and N-H bonding, enhancing mechanical behavior [40,41]. In this study, PGBT may share similar mechanism as BNNT and PLLA is abundant with mentioned moles, but it requires further validations throughout Fourier transform infrared spectroscopy and Raman spectroscopy tests in the future.

Upon implantation, the material interacts with tissue fluids, marking the first step of interaction with the tissue. Good hydrophilicity promotes cell adhesion, proliferation, and differentiation. A smaller contact angle indicates better hydrophilicity. In this experiment, the instantaneous contact angle of both groups of membranes is less than 45° at 5 s, and the liquid completely infiltrates afterwards, demonstrating excellent hydrophilicity. PLLA itself is highly hydrophobic, which is unfavorable for tissue healing [42], while gelatin contains peptide adhesion sequences [43]. By blending gelatin into the raw material, we significantly enhance the overall hydrophilicity of the membrane, and the addition of BNNT does not alter the hydrophilicity.

Initially after implantation, the GBR membrane should remain intact to prevent fibrous tissue ingrowth, then it should gradually degrade after the osteogenesis process is complete. PLLA itself degrades very slowly [42], but the addition of gelatin accelerates the degradation rate. Both the control group and the PGBT group show a degradation rate of approximately 50 % after 30 days of implantation, with the rate gradually slowing down. By day 90, the control group degrades to about 60 %, while the PGBT group reaches about 70 % ($p < 0.5$). This may be due to the partial agglomeration of BNNT, which disrupts the membrane integrity, causing localized weak areas to degrade first. Clinically, the osteogenesis time for alveolar bone defects is about 3 months, which is consistent with the results of this study, proving that the degradation rate of PGBT material is reasonable.

Piezoelectric materials deform under the force of mechanical waves of ultrasound, resulting in changes in their electric potential. In this experiment, we directly connected the fibrous membrane with electrode sheets, integrated it into an electrochemical platform, and applied LIPUS at an intensity of $0.1\text{W}/\text{cm}^2$. The results show that the control group generated a weak potential of approximately 24 mV, while the output voltage of PGBT reached 130 mV. Electrospun PLLA is inherently a piezoelectric polymer material with a crystalline phase of spontaneously polarized asymmetric centers [44], mechanical stimulation triggers the polarization of dipole movement, achieving electroactivity [45]. In this experiment, the control group with pure electrospun PLLA exhibited a low output voltage, consistent with related literature [46]. We attribute the strong piezoelectricity of PGBT to the addition of BNNT. BNNT is a novel polycrystalline piezoelectric ceramic material formed by curling boron nitride, similar in structure to carbon nanotubes. Most polycrystalline piezoelectric ceramics, such as barium titanate, often have their piezoelectric effects between grains cancel each other out, showing no macroscopic piezoelectric effect [47]. Therefore, traditional piezoelectric tissue engineering research first applies an electric field to polarize the material [48]. In clinical practice, ideal biomaterials should meet the characteristics of low operative sensitivity, disposability, and ease of disinfection, but conventional piezo-materials with complex polarization strategy fail to cater to clinical needs. In this study, PGBT shows relatively strong piezoelectric performance without extra polarization after ultrasound stimulation, indicating that PGBT may possess a ferroelectric effect with spontaneous polarization in a regular direction, the orderly molecular arrangement and enhanced piezoelectricity is reported to be attributed to the increased β -phase after nanotubes were added during electrospinning [49,50]. Otherwise, direct piezoforce microscopy data of PGBT membrane are needed to validate the supposition.

The GBR membrane must process good biocompatibility. Our CCK8

results (Fig. 2C) from co-culturing the membrane extract with cells and directly co-culturing each group's membrane with cells show that, regardless of ultrasound stimulation, none of the groups exhibit cytotoxicity to MC3T3-E1 proliferation. Live/dead cell staining (Fig. 2A) indicate that after 3 days all groups maintain good cell viability, with few red fluorescent dead cells observed. In *in vivo* experiments, HE staining of organs and cranial bone sections at 8 weeks also shows no significant inflammatory cell aggregation (Fig. 4A and B), confirming that the material does not adversely affect the tissue. SEM (Fig. 2D) reveal that cells adhere polytonally to the nanofibers, with increased cell adhesion in the PGBT(+) group. This may be due to the electric potential generated by ultrasound stimulation of the material, which initially attracts various proteins, and cells are subsequently drawn to the formed protein layer through adhesion [51]. Additionally, the micro-electrical environment may promote the cells' secretion of extracellular matrix proteins, further altering the local microenvironment [52]. Cell morphology staining (Fig. 2E) shows similar results, with co-cultured cells exhibiting a polygonal shape and intact cytoskeleton, and higher density in the PGBT(+) group. However, once applied *in vivo* BNNT would leak out during the scaffold degradation and make direct impact on tissues, the further mid-term or long-term cytotoxic evaluation is required in future studies.

Our experiment further confirms the osteogenic potential of PGBT combined with LIPUS through *in vitro* ALP and AR staining. In Fig. 2F (a), the dark purple staining indicates areas of calcium deposition, while in Fig. 2F(b), the dark red staining represents newly formed calcium nodules. After 14 days of osteogenic induction differentiation, it is observed that the PGBT(+) group has significantly more ALP dark-stained areas and red calcium nodules compared to the other groups. Quantitative tests show the same results (Fig. G(a,b)), confirming that PGBT(+) promotes osteogenic differentiation of cells.

One of the key factors for the success of GBR surgery is preventing the invasion of fibroblastic tissue post-operation. In this experiment, the NIH3T3-E1 was selected to simulate human fibroblasts. After 14 days, the membrane was not penetrated by the cells, providing a good and stable environment for osteogenesis in defect area.

The oral cavity is a complex environment with bacteria. After surgeries, GBR membranes are often not be able to be fully covered by soft tissue sutures, leaving open areas in direct contact with oral bacteria. Therefore, antibacterial property is one of the goals in constructing novel membranes. In this study, common Gram-negative *E. coli* was co-cultured with the membrane. Both colony counting and CCK-8 results indicate that PGBT + LIPUS has an antibacterial effect, which is in consistent with relative literature [13]. Human eukaryotic cell surfaces are electrically neutral, while bacterial cell membranes are negatively charged [53]. Electric fields emanating from piezo-materials have been demonstrated to induce significant potential differences and oxidative stress at the interface between the materials and bacteria. This phenomenon disrupts cellular membranes and leads to a depletion of sugar-energy resources, thereby effectively inhibiting surface-attached microbial activity [54,55]. Immune cells such as macrophages also play an important role in clearing bacteria, possibly due to the activation of immune regulatory mechanisms by microcurrent stimulation [56].

To investigate the osteogenic potential of the PGBT *in vivo*, we established a rat cranial defect model. Previous studies have suggested that full-thickness cranial defects with a diameter greater than 5 mm are considered critical-sized defects [57], where the animal's self-repair ability is limited, effectively reflecting the osteogenic potential of the material. Therefore, we prepared a 6 mm diameter circular full-thickness cranial defect model and included an LIPUS group (Fig. 3B). Due to the significantly faster growth rate of rats compared to humans, we selected the 4-week point as the early observation period for osteogenesis and the 8-week point for observing mid-to-late bone repair, based on literature. Micro-CT results show that at 4 and 8 weeks, the new bone volume and bone density in the PGBT(+) group are significantly higher than in the other groups (Fig. 4A–C). This is consistent

with the *in vitro* results where the piezoelectric effect activated by LIPUS promotes MC3T3-E1's osteogenic differentiation. Additionally, in the sagittal view (Fig. 4A), the new bone height in the PGBT(+) group at 4 and 8 weeks is significantly higher than in the other groups. Masson staining and quantitative analysis (Fig. 4C and F(a)) reveal same results, showing that the new bone height in the PGBT(+) group is significantly higher. Additionally, although the BV/TV and BMD in the Control(+) group do not significantly differ from the other non-ultrasound groups (Fig. 4F(a)), the osteogenic pattern shows uniformly distributed stained areas with vertical growth. This may be due to LIPUS promoting osteoblast adhesion and the waves making the spatial distribution of cells more uniform. At 8 weeks, the new bone volume in the Blank group is low, indicating poor repair ability for critical-sized bone defects. The new bone formation in the Control(–), Control(+), and PGBT(–) groups is significantly better than in the Blank group, suggesting that the barrier membrane alone can maintain the defect space and ensure limited bone regeneration capacity.

Col-I gene is highly expressed in the early stages of osteogenic differentiation of stem cells, while OCN is a key gene expressed in the late stages of that [58]. In this experiment, we performed immunohistochemical staining to investigate the osteogenic potential of each group's membrane at the protein level. The results show that at 4 weeks, the positive expression of Col-I and OCN in the PGBT(+) group is significantly higher than in the other groups, indicating that the activation of the piezoelectric membrane enhances osteogenic activity in the early stages. At 8 weeks, the expression trend of Col-I in the PGBT(+) group remains consistent, but the expression of OCN significantly decreases, lower than the other groups except for the Blank group. This may be because Col-I primarily marks newly formed collagen, located within the new bone tissue, and is highly expressed at 8 weeks. OCN, on the other hand, is in the cytoplasm and new bone lacunae, and as the bone tissue matures at 8 weeks, the expression of OCN decreases. Additionally, the large amount of new bone tissue occupying the remaining space leads to a reduction in cell and its OCN expression. In the Col-I and OCN staining images of the PGBT(+) group at 8 weeks (Fig. D(b), Fig. E(b)), new bone tissue interweaves with the upper membrane in the defect area, with numerous nanofibers inserted into the new bone. This demonstrates that PGBT, while blocking soft tissue, slowly degrades and significantly promotes bone tissue formation when activated by LIPUS. *In vivo*, cells generate surface charges and intrinsic potentials under physiological conditions, which regulate cellular behavior through signal pathway-mediated biological processes, including calcium signaling, surface receptor redistribution, ATP, and reactive oxygen species (ROS) events. Artificial piezoelectric stimulation can produce bioelectric signals and endogenous electric fields (EnEF) like natural tissues, potentially enhancing osteogenic differentiation and cell activity through similar signaling pathways [59,60].

In this study, we primarily investigate the PGBT membrane with LIPUS and certify its dual function of osteogenesis and antibacterial through *in-vitro* and *in-vivo* experiments. Especially, the unexpected vertical bone healing in cranial defect experiments suggests that SPT with PGBT membrane is promising in the application of vertical bone repair, as convention has long held that vertical alveolar defect is one of the most clinical sensitive challenges in dental implantation and GBR. Human bone is increasingly believed to be an electric-sensitive organ, our results hint that PGBT may exert effect via creating a electric field that activates the bone sensing and promotes regeneration in defect area. However, in this research, potential signaling pathways of PGBT are not explored. We plan to do further investigations to uncover the specific molecular mechanisms, and we have been conducting relevant experiments.

5. Conclusion

In summary, we successfully established a multifunctional piezoelectric GBR membrane, PGBT. Under LIPUS, it promotes osteogenic

differentiation of MC3T3-E1 cells in vitro and enhances bone repair in rat cranial defects in vivo. The incorporation of BNNT enhances the material's elastic modulus, optimizes degradation, and maintains good biocompatibility, especially endowing PGBT with piezoelectric properties, generating an electric potential difference of approximately 130 mV under 0.1W/cm² ultrasound. PGBT significantly promotes MC3T3-E1 adhesion and osteogenic differentiation under LIPUS, while also exhibiting antibacterial properties and barrier functions. In-vivo experiments confirm that PGBT combined with LIPUS demonstrates superior bone repair efficacy. Overall, our results suggest that PGBT with LIPUS may represent a novel strategy for promoting oral bone regeneration.

CRedit authorship contribution statement

Keshi Zhu: Writing – original draft, Methodology, Investigation, Data curation, Conceptualization. **Ruixue Li:** Writing – review & editing, Funding acquisition, Formal analysis. **Shi Yin:** Visualization, Validation, Conceptualization. **Fei Yang:** Writing – review & editing, Funding acquisition. **Yang Sun:** Formal analysis. **Yixiao Xing:** Formal analysis. **Yiling Yang:** Data curation. **Wanjing Xu:** Formal analysis. **Youcheng Yu:** Writing – review & editing, Supervision, Project administration, Funding acquisition.

Declaration of competing interest

The authors declare that they have no known competing financial interests or personal relationships that could have appeared to influence the work reported in this paper.

Acknowledgements

This research was funded by the National Natural Science Foundation of China (82170990, 82401064), Science and Technology Committee of Shanghai (22YF1442900).

Appendix A. Supplementary data

Supplementary data to this article can be found online at <https://doi.org/10.1016/j.mtbio.2024.101418>.

Data availability

Data will be made available on request.

References

- [1] Y. Ren, L. Fan, S. Alkildani, L. Liu, S. Emmert, S. Najman, D. Rimashevskiy, R. Schnettler, O. Jung, X. Xiong, M. Barbeck, Barrier membranes for guided bone regeneration (GBR): a focus on recent advances in collagen membranes, *Int. J. Mol. Sci.* 23 (23) (2022).
- [2] Z. Li, C. Yang, J. Wang, K. Zheng, W. Luo, The application of CGF combined with GBR in alveolar bone increment for patients with anxiety disorder: a rare case report and literature review, *Medicine (Baltim.)* 102 (45) (2023) e35905.
- [3] M. Mohammadkhah, D. Marinkovic, M. Zehn, S. Checa, A review on computer modeling of bone piezoelectricity and its application to bone adaptation and regeneration, *Bone* 127 (2019) 544–555.
- [4] Q. Du, S. Su, H. Dai, Z. Li, Physical biomedical science: a new field of original interdisciplinary research, *Chin. Sci. Bull.* 69 (15) (2024) 2008–2014.
- [5] A.H. Rajabi, M. Jaffe, T.L. Arinze, Piezoelectric materials for tissue regeneration: a review, *Acta Biomater.* 24 (12–23) (2015).
- [6] J. Sun, W. Xie, Y. Wu, Z. Li, Y. Li, Accelerated bone healing via electrical stimulation, *Adv. Sci.* (2024) e2404190.
- [7] D. D'Alessandro, C. Ricci, M. Milazzo, G. Strangis, F. Forli, G. Buda, M. Petrini, S. Berrettini, M.J. Uddin, S. Danti, P. Parchi, Piezoelectric signals in vascularized bone regeneration, *Biomolecules* 11 (11) (2021).
- [8] N. More, G. Kapusetti, Piezoelectric material - a promising approach for bone and cartilage regeneration, *Med. Hypotheses* 108 (2017) 10–16.
- [9] Y. Shang, C. Huang, Z. Li, X. Du, Bioinspired ultra-stretchable and highly sensitive structural color electronic skins, *Adv. Funct. Mater.* (2024) 2412703.
- [10] X. Wang, X. Dai, Y. Chen, Sonopiezoelectric nanomedicine and materdicine, *Small* 19 (29) (2023) e2301693.
- [11] Y. Bai, H. Meng, Z. Li, Z.L. Wang, Degradable piezoelectric biomaterials for medical applications, *Med Mat* 1 (1) (2024) 40–49.
- [12] L. Jing, F. Zhuang, W. Feng, H. Huang, Y. Chen, B. Huang, Doping-engineered piezoelectric ultrathin nanosheets for synergistically piezo-chemocatalytic antitumor and antibacterial therapies against cutaneous melanoma, *Small* (2024) e2401171.
- [13] E.O. Carvalho, T. Marques-Almeida, B.D.D. Cruz, D.M. Correia, J. Esperanca, I. Iraztorza, U. Silvan, M.M. Fernandes, S. Lanceros-Mendez, C. Ribeiro, Piezoelectric biomaterials with embedded ionic liquids for improved orthopedic interfaces through osseointegration and antibacterial dual characteristics, *Biomater. Adv.* 164 (2024) 213970.
- [14] S.M. Damaraju, Y. Shen, E. Elele, B. Khusid, A. Eshghinejad, J. Li, M. Jaffe, T. L. Arinze, Three-dimensional piezoelectric fibrous scaffolds selectively promote mesenchymal stem cell differentiation, *Biomaterials* 149 (51–62) (2017).
- [15] Y. Tang, C. Wu, Z. Wu, L. Hu, W. Zhang, K. Zhao, Fabrication and in vitro biological properties of piezoelectric bioceramics for bone regeneration, *Sci. Rep.* 7 (2017) 43360.
- [16] R. Sobreiro-Almeida, M.N. Tamano-Machiavello, E.O. Carvalho, L. Cordon, S. Doria, L. Senent, D.M. Correia, C. Ribeiro, S. Lanceros-Mendez, I.S.R. Sabater, J. L. Gomez Ribelles, A. Sempere, Human mesenchymal stem cells growth and osteogenic differentiation on piezoelectric poly(vinylidene fluoride) microsphere substrates, *Int. J. Mol. Sci.* 18 (11) (2017).
- [17] A. Mirzaei, E. Saburi, S.E. Enderami, M. Barati Bagherabad, S.E. Enderami, M. Chokami, A. Shapouri Moghadam, R. Salarinia, A. Ardeshirylajimi, V. Mansouri, F. Soleimanifar, Synergistic effects of polyaniline and pulsed electromagnetic field to stem cells osteogenic differentiation on polyvinylidene fluoride scaffold, *Artif. Cells, Nanomed. Biotechnol.* 47 (1) (2019) 3058–3066.
- [18] J.H. Kang, G. Sauti, C. Park, V.I. Yamakov, K.E. Wise, S.E. Lowther, C.C. Fay, S. A. Thibeault, R.G. Bryant, Multifunctional electroactive nanocomposites based on piezoelectric boron nitride nanotubes, *ACS Nano* 9 (12) (2015) 11942–11950.
- [19] S.V. Anandhan, U.M. Krishnan, Boron nitride nanotube scaffolds: emergence of a new era in regenerative medicine, *Biomed Mater* 16 (4) (2021).
- [20] G.G. Genchi, E. Sinibaldi, L. Ceseracciu, M. Labardi, A. Marino, S. Marras, G. De Simoni, V. Mattoli, G. Ciofani, Ultrasound-activated piezoelectric P(VDF-TrFE)/boron nitride nanotube composite films promote differentiation of human SaOS-2 osteoblast-like cells, *Nanomedicine* 14 (7) (2018) 2421–2432.
- [21] X. Li, X. Wang, X. Jiang, M. Yamaguchi, A. Ito, Y. Bando, D. Golberg, Boron nitride nanotube-enhanced osteogenic differentiation of mesenchymal stem cells, *J. Biomed. Mater. Res. B Appl. Biomater.* 104 (2) (2016) 323–329.
- [22] D. Lahiri, F. Rouzaud, T. Richard, A.K. Keshri, S.R. Bakshi, L. Kos, A. Agarwal, Boron nitride nanotube reinforced polylactide-polycaprolactone copolymer composite: mechanical properties and cytocompatibility with osteoblasts and macrophages in vitro, *Acta Biomater.* 6 (9) (2010) 3524–3533.
- [23] D. Lahiri, V. Singh, A.P. Benaduce, S. Seal, L. Kos, A. Agarwal, Boron nitride nanotube reinforced hydroxyapatite composite: mechanical and tribological performance and in-vitro biocompatibility to osteoblasts, *J. Mech. Behav. Biomed. Mater.* 4 (1) (2011) 44–56.
- [24] A. Salvetti, L. Rossi, P. Iacopetti, X. Li, S. Nitti, T. Pellegrino, V. Mattoli, D. Golberg, G. Ciofani, In vivo biocompatibility of boron nitride nanotubes: effects on stem cell biology and tissue regeneration in planarians, *Nanomedicine (Lond)* 10 (12) (2015) 1911–1922.
- [25] D. Lahiri, V. Singh, A.K. Keshri, S. Seal, A. Agarwal, Apatite formability of boron nitride nanotubes, *Nanotechnology* 22 (20) (2011) 205601.
- [26] G.G. Genchi, G. Ciofani, Bioapplications of boron nitride nanotubes, *Nanomedicine (Lond)* 10 (22) (2015) 3315–3319.
- [27] A.A. Aldana, G.A. Abraham, Current advances in electrospun gelatin-based scaffolds for tissue engineering applications, *Int J Pharm* 523 (2) (2017) 441–453.
- [28] A.S. Pryadko, V.V. Botvin, Y.R. Mukhortova, I. Pariy, D.V. Wagner, P.P. Laktionov, V.S. Chernonosova, B.P. Chelobanov, R.V. Chernozem, M.A. Surmeneva, A. L. Kholkin, R.A. Surmenev, Core-shell magnetoactive PHB/Gelatin/Magnetite composite electrospun scaffolds for biomedical applications, *Polymers* 14 (3) (2022).
- [29] M. Polak, K. Berniak, P.K. Szewczyk, J.E. Karbowiczek, M.M. Marzec, U. Stachewicz, Plla scaffolds with controlled surface potential and piezoelectricity for enhancing cell adhesion in tissue engineering, *Appl. Surf. Sci.* 621 (1) (2023) 156835.
- [30] X. Cui, L. Xu, Y. Shan, J. Li, J. Ji, E. Wang, B. Zhang, X. Wen, Y. Bai, D. Luo, C. Chen, Z. Li, Piezocatalytically-induced controllable mineralization scaffold with bone-like microenvironment to achieve endogenous bone regeneration, *Sci. Bull.* 69 (12) (2024) 1895–1908.
- [31] Q. Yu, Y. Bai, Z. Li, F. Jiang, R. Luo, Y. Gai, Z. Liu, L. Zhou, Y. Wang, C. Li, Interface-induced high piezoelectric γ -glycine-based flexible biodegradable films, *Nano Energy* 121 (2024).
- [32] I.O. Pariy, R. Chernozem, P.V. Chernozem, Y.R. Mukhortova, A. Skirtach, V. Shvartsman, D. Lupascu, M. Surmenev, S. Mathur, R. Surmenev, Hybrid biodegradable electrospun scaffolds based on poly(L-lactic acid) and reduced graphene oxide with improved piezoelectric response, *Polym. J.* 54 (2022) 1237–1252.
- [33] A.P. Rickel, X. Deng, D. Engebretson, Z. Hong, Electrospun nanofiber scaffold for vascular tissue engineering, *Mater Sci Eng C Mater Biol Appl* 129 (2021) 112373.
- [34] H.S. Sofi, A. Abdal-Hay, S. Ivanovski, Y.S. Zhang, F.A. Sheikh, Electrospun nanofibers for the delivery of active drugs through nasal, oral and vaginal mucosa: current status and future perspectives, *Mater Sci Eng C Mater Biol Appl* 111 (2020) 110756.

- [35] A. Moussa, S. Deridder, K. Broeckhoven, G. Desmet, Computational fluid dynamics study of the dispersion caused by capillary misconnection in nano-flow liquid chromatography, *Anal. Chem.* 95 (37) (2023) 13975–13983.
- [36] M.M. Eldokmak, M.M. Essawy, S. Abdelkader, S. Abolghait, Bioinspired polydopamine/nano-hydroxyapatite: an upgrading biocompatible coat for 3D-printed polylactic acid scaffold for bone regeneration, *Odontology* (2024 May 21), <https://doi.org/10.1007/s10266-024-00945-x>. Published online.
- [37] C. Feng, Y. Li, M. Gu, W. Li, Y. Yang, S. Chen, Y. Ma, D. Geng, L. Xiao, Z. Wang, The dopamine D1 receptor attenuates titanium particle-induced inhibition of osteogenesis by activating the wnt signaling pathway, *Mediators Inflamm* (2023) 6331650.
- [38] Y. Yu, X. Li, J. Li, D. Li, Q. Wang, W. Teng, Dopamine-assisted co-deposition of hydroxyapatite-functionalised nanoparticles of polydopamine on implant surfaces to promote osteogenesis in environments with high ROS levels, *Mater Sci Eng C Mater Biol Appl* 131 (2021) 112473.
- [39] I. Elgali, O. Omar, C. Dahlin, P. Thomsen, Guided bone regeneration: materials and biological mechanisms revisited, *Eur. J. Oral Sci.* 125 (5) (2017) 315–337.
- [40] S. Wu, T. Dong, Y. Li, M. Sun, Y. Qi, J. Liu, M.A. Kuss, S. Chen, B. Duan, State-of-the-art review of advanced electrospun nanofiber yarn-based textiles for biomedical applications, *Appl. Mater. Today* 27 (2022) 101473.
- [41] J. Macossay, F.A. Sheikh, T. Cantu, T.M. Eubanks, M.E. Salinas, C.S. Farhangi, H. Ahmad, M.S. Hassan, M.S. Khil, S.K. Maffi, H. Kim, G.L. Bowlin, Imaging, spectroscopic, mechanical and biocompatibility studies of electrospun tecoflex (R) EG 80A nanofibers and composites thereof containing multiwalled carbon nanotubes, *Appl. Surf. Sci.* 321 (2014) 205–213.
- [42] J. Rajewska, J. Kowalski, J. Matys, M. Dobrzynski, R.J. Wiglusz, The use of lactide polymers in bone tissue regeneration in dentistry-A systematic review, *J. Funct. Biomater.* 14 (2) (2023).
- [43] X. Zhou, Z. Luo, A. Baidya, H.J. Kim, C. Wang, X. Jiang, M. Qu, J. Zhu, L. Ren, F. Vajhadin, P. Tebon, N. Zhang, Y. Xue, Y. Feng, C. Xue, Y. Chen, K. Lee, J. Lee, S. Zhang, C. Xu, N. Ashammakhi, S. Ahadian, M.R. Dokmeci, Z. Gu, W. Sun, A. Khademhosseini, Biodegradable beta-cyclodextrin conjugated gelatin methacryloyl microneedle for delivery of water-insoluble drug, *Adv Healthc Mater* 9 (11) (2020) e2000527.
- [44] Y. Liu, G. Dzditor, T.T. Le, T. Vinikoor, K. Morgan, E.J. Curry, R. Das, A. McClinton, E. Eisenberg, L.N. Apuzzo, K.T.M. Tran, P. Prasad, T.J. Flanagan, S. W. Lee, H.M. Kan, M.T. Chorsi, K.W.H. Lo, C.T. Laurencin, T.D. Nguyen, Exercise-induced piezoelectric stimulation for cartilage regeneration in rabbits, *Sci. Transl. Med.* 14 (627) (2022) eabi7282.
- [45] Ali Faizan, Raza Waseem, Li Xilin, Gul Hajera, Ki Hyun, Piezoelectric energy harvesters for biomedical applications, *Nano Energy* 57 (2019) 879–902.
- [46] X. Lu, C. Sun, L. Chen, Z. Feng, H. Gao, S. Hu, M. Dong, J. Wang, W. Zhou, N. Ren, H. Zhou, H. Liu, Stemness maintenance and massproduction of neural stem cells on poly L-lactic acid nanofibrous membrane based on piezoelectriceffect, *Small* 18 (13) (2022) 2107236.
- [47] J. Guo, W. Chen, H. Chen, Y. Zhao, Y. Zhang, Recent progress in optical control of ferroelectric polarization, *Adv. Opt. Mater.* 23 (9) (2021) 2002146.
- [48] B. Cromwell, M. Dubnicka, L. Sumathirathne, A. Thach, W.B. Euler, Mechanistic study of rhodamine B piezocatalytic decomposition using poly(vinylidene difluoride) and related polymers, *J. Phys. Chem. C* 127 (25) (2023) 11940–11947.
- [49] Y. Su, W. Li, X. Cheng, Y. Zhou, S. Yang, X. Zhang, C. Chen, T. Yang, H. Pan, G. Xie, G. Chen, X. Zhao, X. Xiao, B. Li, H. Tai, Y. Jiang, L.Q. Chen, F. Li, J. Chen, High-performance piezoelectric composites via beta phase programming, *Nat. Commun.* 13 (1) (2022) 4867.
- [50] A. Huang, Y. Zhu, S. Peng, B. Tan, X. Peng, Improved energy harvesting ability of single-layer binary fiber nanocomposite membrane for multifunctional wearable hybrid piezoelectric and triboelectric nanogenerator and self-powered sensors, *ACS Nano* 18 (1) (2024) 691–702.
- [51] J. Barberi, S. Spriano, Titanium and protein adsorption: an overview of mechanisms and effects of surface features, *Materials* 14 (7) (2021).
- [52] D. Harjanto, M.H. Zaman, Matrix mechanics and receptor-ligand interactions in cell adhesion, *Org. Biomol. Chem.* 8 (2) (2010) 299–304.
- [53] S. Elia, P. Lamberti, V. Tucci, Influence of uncertain electrical properties on the conditions for the onset of electroporation in an eukaryotic cell, *IEEE Trans. NanoBioscience* 9 (3) (2010) 204–212.
- [54] R. Gaupp, N. Ledala, G.A. Somerville, Staphylococcal response to oxidative stress, *Front. Cell. Infect. Microbiol.* 2 (33) (2012).
- [55] W. Xu, Y. Yu, K. Li, L. Shen, X. Liu, Y. Chen, J. Feng, W. Wang, W. Zhao, J. Shao, B. Ma, J. Wu, S. Ge, H. Liu, J. Li, Surface-confined piezocatalysis inspired by ROS generation of mitochondria respiratory chain for ultrasound-driven noninvasive elimination of implant infection, *ACS Nano* 17 (10) (2023) 9415–9428.
- [56] M. Sun, J. Wang, X. Huang, R. Hang, P. Han, J. Guo, X. Yao, P.K. Chu, X. Zhang, Ultrasound-driven radical chain reaction and immunoregulation of piezoelectric-based hybrid coating for treating implant infection, *Biomaterials* 307 (2024) 122532.
- [57] L.C. Torquato, E.A.C. Suarez, D.V. Bernardo, I.L.R. Pinto, L.O. Mantovani, T.I. L. Silva, M.A.N. Jardim, M.P. Santamaria, A.C. De Marco, Bone repair assessment of critical size defects in rats treated with mineralized bovine bone (Bio-Oss(R)) and photobiomodulation therapy: a histomorphometric and immunohistochemical study, *Lasers Med Sci* 36 (7) (2021) 1515–1525.
- [58] B.J. Zhang, L. He, Z.W. Han, X.G. Li, W. Zhi, W. Zheng, Y.D. Mu, J. Weng, Enhanced osteogenesis of multilayered pore-closed microspheres-immobilized hydroxyapatite scaffold via sequential delivery of osteogenic growth peptide and BMP-2, *J. Mater. Chem. B* 5 (41) (2017) 8238–8253.
- [59] Y. Zhang, J. Tang, W. Fang, Q. Zhao, X. Lei, J. Zhang, J. Chen, Y. Li, Y. Zuo, Synergetic effect of electrical and topographical cues in aniline trimer-based polyurethane fibrous scaffolds on tissue regeneration, *J. Funct. Biomater.* 14 (4) (2023).
- [60] N. Bhaskar, M.C. Kachappilly, V. Bhusan, H.J. Pandya, B. Basu, Electrical field stimulated modulation of cell fate of pre-osteoblasts on PVDF/BT/MWCNT based electroactive biomaterials, *J. Biomed. Mater. Res.* 111 (3) (2023) 340–353.